Research Article | Vol. 30, No. 18 / 29 Aug 2022 / Optics Express 32292
Optics EXPRESS

Coupling light emission of single-photon sources into single-mode fibers: mode matching, coupling efficiencies, and thermo-optical effects

JULIAN SCHWAB,[1,*] KSENIA WEBER,[1] JOHANNES DROZELLA,[2] CARLOS JIMENEZ,[2] ALOIS HERKOMMER,[2] LUCAS BREMER,[3] STEPHAN REITZENSTEIN,[3] AND HARALD GIESSEN[1]

[1]*4th Physics Institute and Research Center SCoPE, University of Stuttgart, 70569 Stuttgart, Germany*
[2]*Institute for Applied Optics (ITO) and Research Center SCoPE, University of Stuttgart, 70569 Stuttgart, Germany*
[3]*Institute of Solid State Physics, Technische Universität Berlin, 10623 Berlin, Germany*
[*]*julian.schwab@pi4.uni-stuttgart.de*

Abstract: We discuss the coupling efficiency of single-photon sources into single-mode fibers using 3D printed micro-optical lens designs. Using the wave propagation method, we optimize lens systems for two different quantum light sources and assess the results in terms of maximum coupling efficiencies, misalignment effects, and thermo-optical influences. Thereby, we compare singlet lens designs with one lens printed onto the fiber with doublet lens designs with an additional lens printed onto the semiconductor substrate. The single-photon sources are quantum dots based on microlenses and circular Bragg grating cavities at 930 nm and 1550 nm, respectively.

© 2022 Optica Publishing Group under the terms of the Optica Open Access Publishing Agreement

1. Introduction

The real-world implementation of quantum communication technologies [1,2] such as quantum repeater networks [3–5] or quantum key distribution [6,7] requires single photons emitted deterministically by two-level systems to be collected into the same spatio-temporal mode [8,9]. This necessitates the use of single-mode optical fibers in which the photons have to be coupled reliably and efficiently [10–12].

Non-classical single-photon sources (SPSs) which are suitable for applications in quantum technologies [13] include NV [14,15] and SiV [16] centers in diamond, localized emitters in 2D quantum materials [17], trapped single atoms [18] or ions [19], and semiconductor quantum dots (QDs) [20–22]. This work focuses on SPSs based on semiconductor QDs which have been proven to be practically relevant and to exhibit close-to-ideal emission properties at the required wavelengths in the telecom O-band [23] and C-band [20,24–28]. We here consider nanophotonic structures which were presented in Ref. [29] and are based on InAs/In(Ga)As QDs that were optimized for maximum photon extraction efficiency and Gaussian-like emission characteristics.

Powerful solutions are required to realize efficient fiber coupling of SPS. The efficiency of near-field fiber coupling, where the fiber is usually in direct contact with the structure, is mainly limited by poor mode matching between the emitter and the fiber [30–32]. To avoid this problem, far-field coupling with additional micro-optical elements can be used. As schematically shown in Fig. 1(a), optical elements are used to match the emitted mode of the SPS to the fiber-mode.

The fabrication of micro-optical elements is made possible by femtosecond 3D printing which has become a versatile and successful technology for manufacturing nano- and microscopic structures [33–36]. First results using this approach were reported in Ref. [37,38]. Besides the printing of the lens design, the fiber coupling procedure also includes the printing of a fiber

#465101 https://doi.org/10.1364/OE.465101
Journal © 2022 Received 24 May 2022; revised 8 Jul 2022; accepted 22 Jul 2022; published 18 Aug 2022

Optics EXPRESS

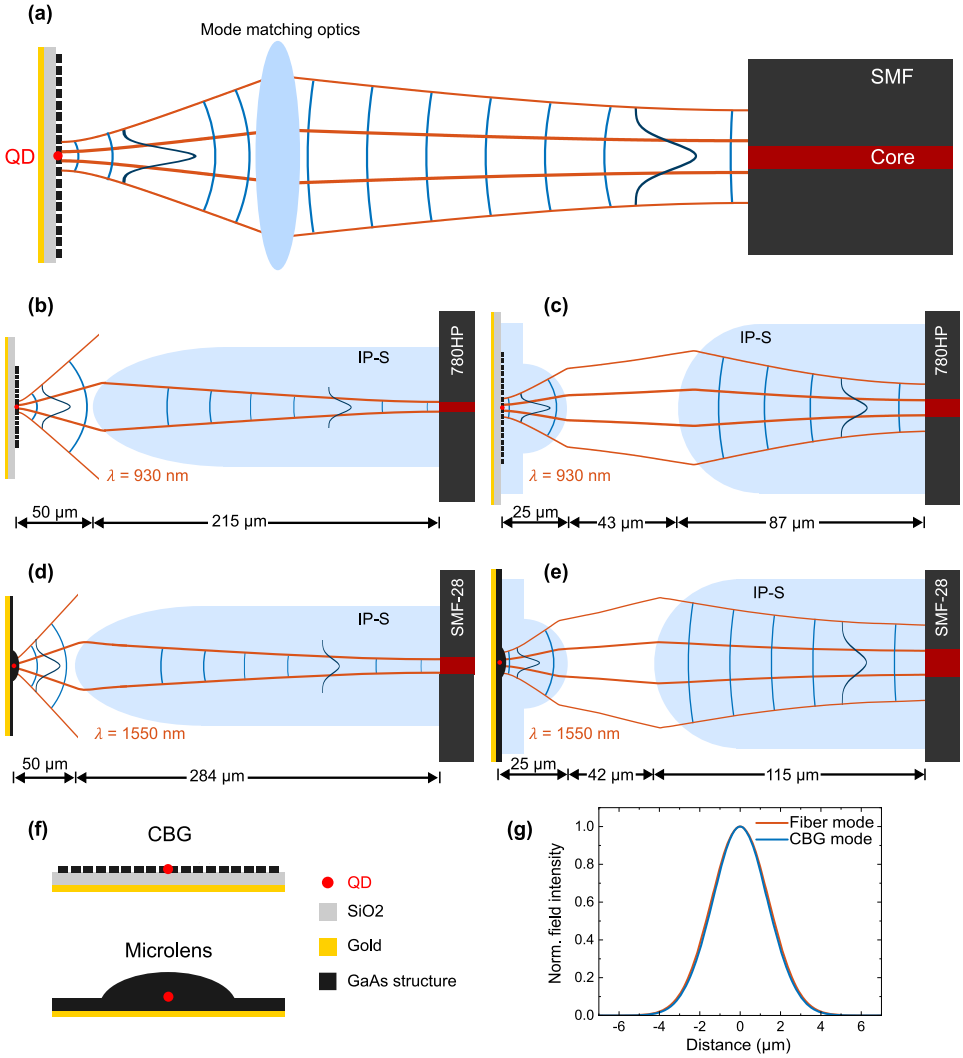

Fig. 1. (a) Illustration of optical elements used for far field coupling of a single-photon source to a single-mode fiber. An ideal lens design perfectly matches the emitted mode of the source with the mode of the fiber. All modes are approximated by Gaussian beams. The blue lines represent the curvature of the wavefronts, and the orange lines are the beam radii. The inner orange line represents the position at which the intensity has dropped by $1/e^2$ while the outer orange line represents the position at which the intensity has dropped by 99%. (b)–(e) Schematic illustration of the discussed lens designs for the microlens and circular Bragg grating photon sources pictured in (f). Each lens design consists of a fiber lens printed directly onto the single-mode fiber. In the case of the doublet lens designs ((c) and (e)) an additional substrate lens is printed onto the substrate. The lens designs are optimized so that the overlap of the in-coupling mode and the fiber mode at the position of the fiber tip is maximized. (g) Exemplary mode overlap for the circular Bragg grating emitter and the doublet lens design.

Optics EXPRESS

holder on the semiconductor substrate which is used to accurately position and fix the optical fiber.

In the past, two different kinds of mode matching optics were introduced. The first is a singlet, in which a lens is printed directly onto the fiber. This approach is schematically illustrated in Figs. 1(b) and (d). It can be seen that the large emission angle of the sources limits the amount of light that can be collected by the optical elements. It should be noted that it is not possible to simply enlarge the overall size of the lens, as one is limited by the curvature required to achieve the necessary NA matching with the fiber.

This issue can be avoided by using a second approach, in which an additional positive lens is printed directly onto the semiconductor substrate. As shown in Figs. 1(c) and (d), this results in a reduced divergence of the emitted mode.

In the following we present a simulation method that can be used to test and optimize lens designs for maximum coupling efficiencies and test their performance after introducing various forms of misalignments and temperature differences. The results are then compared for the different lens designs and SPSs.

2. Theory

In this section the theoretical background behind the numerical simulations and the analytical results are discussed.

2.1. Gaussian optics

The electric field amplitude of a circular Gaussian beam propagating along z-direction is given by

$$E(\rho, z) = \sqrt{\frac{2}{\pi}} \frac{1}{w(z)} \exp\left(\frac{-\rho^2}{w(z)^2}\right) \exp\left[-i\left(k\frac{\rho^2}{2R(z)} + kz - \psi(z)\right)\right], \tag{1}$$

where ρ is the radius in cylindrical coordinates, $\psi(z)$ is the Gouy phase and $k = 2\pi/\lambda$ with the wavelength λ [39,40]. The evolving beam radius is defined by

$$w(z) = w_0\sqrt{1 + \left(\frac{z}{z_\mathrm{R}}\right)^2} \tag{2}$$

and the radius of curvature of the wavefronts is

$$R(z) = z + \frac{z_\mathrm{R}^2}{z}, \tag{3}$$

with the beam waist radius w_0 and the Rayleigh range $z_\mathrm{R} = \pi w_0^2/\lambda$. The numerical aperture of a Gaussian beam is given by

$$\mathrm{NA} = n\sin\theta = n\sin\left[\arctan\left(\frac{\lambda}{\pi w_0}\right)\right], \tag{4}$$

with the half angle of divergence θ. Another way to describe Gaussian beams is via the complex q-parameter

$$q(z) = z + iz_\mathrm{R} = \left[\frac{1}{R(z)} - i\frac{\lambda}{\pi w^2(z)}\right]^{-1} \tag{5}$$

that can be transformed using ray transfer matrix analysis. This allows the computation of the beam parameters at any given point and can also be used to define the radius of curvature of an interface so that the beam behind the interface has a specific beam waist. Thereby, the Lagrangian invariant $nw_0\theta$ is conserved [41].

Optics EXPRESS

2.2. Wave propagation method

While the ABCD formalism can be used to design lens systems with one or more spherical interfaces, aberrations or diffraction are not considered. Therefore, a different method for accurate optimization and testing of the lens design is necessary. For these purposes, the wave propagation method (WPM) is used. Here, we rely on the Hankel-WPM [42] which uses a rotationally symmetric formulation of the original WPM [43]. This method provides accurate results, overcoming the thin-element approximation with increased computational performance and reduced memory requirements due to the exploitation of symmetry which allows for a reduction into two dimensions. This fast method of wave optical simulation only describes the evolution of the scalar field unidirectionally and neglects back-reflected field components.

2.3. Alignment of Gaussian beams

The electric field guided inside a single-mode fiber can be well approximated by a Gaussian intensity distribution and the out-coming beam of a fiber can therefore be described by a Gaussian beam, with the beam waist positioned at the fiber tip [44]. This means that the procedure of coupling a Gaussian beam into a single-mode fiber is equivalent to an alignment of the two Gaussian modes and that surrounding structures like the semiconductor and the fiber themselves do not need to be included in this approach. From here it follows that if the emitted mode of the source can be mode-matched to be equivalent to the fiber mode, the coupling efficiency would be 100%. This implies a great potential for SPSs that emit a Gaussian-like mode. The coupling efficiency of two modes can be calculated using the overlap integral

$$T_\mathrm{g} = \left| \iint E^* E' \,\mathrm{d}x\mathrm{d}y \right|^2 , \tag{6}$$

where E and E' denote the in-coupling mode and the mode of the fiber and E^* is the complex conjugate field. The two modes are given by Eq. (1), where both modes exhibit the same wavelength. It should be noted that for ideal Gaussian beams - without considering aberrations and diffraction - the z-position of the x-y plane in which the overlap integral is evaluated can be chosen freely.

A mismatch can occur if the spot sizes of the modes are different, or when one of the modes is tilted or shifted with respect to the other one. Furthermore, a mismatch can also occur due to deviations from an ideal Gaussian beam, for example as a result of optical aberrations or diffraction. However, this case is not considered in the analytical results. Instead, misalignments are introduced by shifting and tilting one of the modes with respect to the other one. For small angles θ, the electric field can then be expressed as [45]

$$E' = \sqrt{\frac{2}{\pi}} \frac{1}{w_0'} \exp\left[-\frac{(x-d)^2 + y^2}{w'(z-z_0')^2} \right] \exp\left[-ik \left(\theta(x-d) + \frac{(x-d)^2 + y^2}{2R'(z-z_0')} \right) \right]. \tag{7}$$

The analytical results of the overlap integral with these misalignments were originally calculated in Ref. [45,46]. The coupling losses coupling losses due to axial shift (s) and lateral shift (d) or tilt (θ) are considered according to $T_\mathrm{g} = T_\mathrm{ideal} \cdot T_s \cdot T_d \cdot T_\theta$. With $\theta = d = 0$ one obtains

$$T_\mathrm{g} = \frac{4}{(\frac{w_0'}{w_0} + \frac{w_0}{w_0'})^2 + \frac{s^2}{z_\mathrm{R} z_\mathrm{R}'}} \approx T_\mathrm{ideal} \cdot T_s = \frac{4}{(\frac{w_0'}{w_0} + \frac{w_0}{w_0'})^2} \cdot \exp\left(-\frac{4s^2}{k^2 (w_0^2 + w_0'^2)^2} \right), \tag{8}$$

where $s = z_0 - z_0'$ is the distance between the beam waists of the modes. Now a tilt of the fiber by the angle θ is introduced. The plane in which the tilt occurs is called the alignment plane. By

Optics EXPRESS

solving the overlap integral at the alignment plane, so that no additional offset arises, one can show that the coupling efficiency is reduced by a factor of

$$T_\theta = \exp\left[-\frac{\theta^2 T_a}{2}\left(\frac{\pi^2}{\lambda^2}\left(w_0^2 + w_0'^2\right) + \left(\frac{z^2}{w_0^2} + \frac{z'^2}{w_0'^2}\right)\right)\right], \tag{9}$$

where z and z' are the distances between the two beam waists and the alignment plane. When the projection plane - where the overlap integral is evaluated - is chosen differently, an additional offset needs to be added. The effect of an offset on the coupling efficiency can be calculated by assuming an infinitesimal tilt at an infinite distance and defining $d = z\theta$. This yields

$$T_d = \exp\left[-\frac{d^2 T_a}{2}\left(\frac{1}{w_0^2} + \frac{1}{w_0'^2}\right)\right]. \tag{10}$$

From Eqs. (8), (9), and (10) it follows that larger beam waists result in lower losses due to lateral or longitudinal offsets. A tilt, close to the position of the beam waists, results in higher losses for larger beam waists. However, when the alignment plane is more distant to the beam waists the lateral offset that is created by the tilt becomes more dominant. Therefore, in this case the tilt then results in lower losses for larger beam waists.

2.4. Single-photon sources

All relevant parameters regarding the sources and the single-mode fibers are listed in Table 1. In principle, all emitters can be implemented in the simulation. However, while smaller emission angles generally result in higher coupling efficiencies, the effects of different misalignments are mainly influenced by the selected lens design and the fiber which is chosen according to the wavelength. We therefore only show the results for a CBG emitter at 930 nm and the microlens emitter at 1550 nm exemplarily. Additionally, we provide the results of both emitters at the corresponding other wavelength in Supplement 1. The corresponding single-mode fibers supporting these wavelengths were chosen as Thorlabs SM 780 HP and SMF 28. The parameters of the discussed sources were provided by simulations presented in Ref. [29]. While sources such as the CBG emit a rather Gaussian-like mode, some other emitters like the microlens exhibit somewhat of a deviation from a Gaussian distribution. Nevertheless, all modes are approximated by the closest circular Gaussian beam in the following discussion. This results in an overestimation of the coupling efficiency in comparison to a full simulation that includes the propagation of the emitted light of the QD in the semiconductor substrate. However, this method is still useful for our purposes, which are to design lens systems and test the effects of misalignments. The parameters of the source are obtained from the half angle of divergence of the far field emission using Eq. (4). Since rotationally symmetric emission characteristics are expected, we use the mean value of the half angle of divergence for these calculations.

Table 1. Relevant emission parameters of the two single-photon sources and corresponding fibers.

	λ (nm)	w_0(µm)	NA	fiber	$w_{0,\mathrm{fiber}}$(µm)	$\mathrm{NA}_{\mathrm{fiber}}$
Circular Bragg grating on QD	930	1.08	0.264	780 HP	2.87	0.103
Microlens on QD	1550	1.45	0.32	SMF 28	5.20	0.094

3. Simulation and results

3.1. Evaluation of coupling efficiency

In order to evaluate the coupling efficiency of different optics, the far field of the light-source first needs to be propagated through the respective lens systems using the WPM as shown in

Optics EXPRESS

Fig. 2(a). Here it is assumed that the field of the SPS is given by an ideal Gaussian emitter located at the interface between GaAs and air. The coupling efficiency is then calculated by numerically solving the overlap integral of Eq. (6) at the position of the fiber tip.

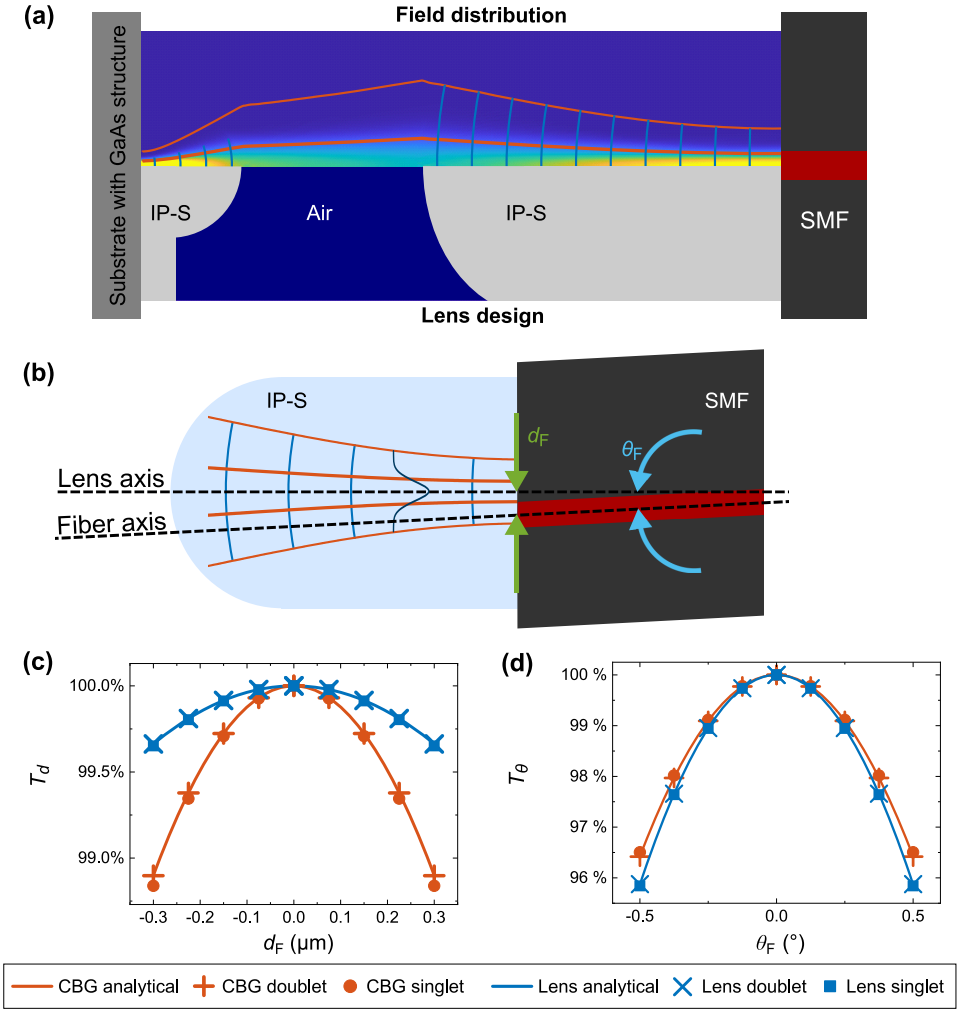

Fig. 2. (a) Simulation result obtained from the wave propagation method in the case of the doublet lens design and a circular Bragg grating (CBG) emitter. The field distribution in the upper half shows the absolute value of the electric field and the lower half schematically shows the lens design. (b) Illustration of the two possible misalignments (lateral offset d_F and tilt θ_F between the two elements). (c), (d) Normalized coupling efficiency for the circular Bragg grating (CBG) and microlens (lens) emitters as a function of the lateral offset (c) and the tilt (d) of the fiber relative to the fiber lens.

3.2. *Creating lens designs with optimized coupling efficiencies*

For each photon source, an ideal singlet and doublet lens design were created. The four different lens designs are schematically shown in Figs. 1(b)-(e).

Each aspheric interface of the lens designs is described by relevant parameters. For each lens design individually, these parameters are optimized for maximum coupling efficiency using the WPM. For doublet lens designs the matrix formalism is used as an ideal starting point for

Optics EXPRESS

the optimization. The detailed steps of the optimization as well as the resulting parameters are provided in Supplement 1. The resulting coupling efficiencies are listed in Table 2. It can be noticed that emitters with a larger NA result in a larger fiber lens for a fixed emitter-fiber lens distance and lower coupling efficiency as a larger portion of the beam does not impinge on the lenses. Additionally, a lower NA of the fiber also ensures higher coupling efficiencies, especially for singlet lens designs. This is due to the reduced curvature of the lens and becomes apparent by comparing the values of all different emitters. The supporting data for that is listed in Supplement 1.

Table 2. Optimized ideal coupling efficiencies without any misalignments and estimated coupling efficiencies that include typical, worse-case (values between typical and worst-case) and worst-case misalignments using the singlet and doublet lens designs for the circular Bragg grating (CBG) and microlens emitters.[a]

	CBG doublet	Microlens doublet	CBG singlet	Microlens singlet
T_{ideal} (%)	99.9	99.8	96.4	92.6
T_{typical} (%)	94.0	95.6	28.4	52.0
$T_{\text{worse-case}}$ (%)	83.5	87.7	1.1	8.6
$T_{\text{worst-case}}$ (%)	68.2	73.2	0.3	0.7

[a]Typical (worse-case) misalignments that are considered in the results include $d_{\text{F}} = 0.1\,\mu\text{m}\,(0.15\,\mu\text{m})$, $\theta_{\text{F}} = 0.2°(0.3°)$, $s_{\text{L}} = 1.5\,\mu\text{m}\,(3\,\mu\text{m})$, $\theta_{\text{L}} = 0.3°\,(0.45°)$, as well as $d_{\text{L1}} = 0.1\,\mu\text{m}\,(0.15\,\mu\text{m})$ and $d_{\text{L2}} = 0.5\,\mu\text{m}\,(1\,\mu\text{m})$ for doublet and $d_{\text{L}} = 1\,\mu\text{m}\,(2\,\mu\text{m})$ for singlet lens designs. The misalignment values for the worst-case coupling efficiencies correspond to the largest misalignment values shown in Figs. 2 and 3.

3.3. Misalignments

During the printing and alignment process, various deviations can occur. Their effect on the coupling efficiency is discussed in the following.

Misalignments of the fiber relative to the fiber lens printed on top of it are shown in Fig. 2(b). A lateral offset can occur when the fiber lens is not perfectly centered on the fiber core and instead is offset by a value of d_{F}. This offset can for instance arise from misalignments in the printing process. Typically these type of offsets are around 100 nm and do not exceed 300 nm in size [47]. Additionally, it might be the case that the fiber is not cleaved perfectly perpendicular to the core. In that case, the lens will be printed on the slightly tilted surface which results in a tilt angle θ_{F} between fiber and lens. Using precise cleaving equipment, typical cleaving angles are around 0.2° and do not exceed 0.5° [48,49]. Thereby it is important, that the output mode of the fiber is tilted according to Snell's law. For in-coupling modes propagating along the lens axis, this results in a tilt of approximately $3\theta_{\text{F}}/2$ between the fiber mode and the in-coupling mode that is considered in the results.

The numerical solutions for the coupling efficiencies are obtained by solving the overlap integral of Eq. (6) numerically at the position of the fiber tip. A lateral offset can be added by shifting one of the modes by the value of d and a tilt can be added by multiplying one of the modes by a factor of $\exp(ik\theta x)$ as in Eq. (7) before computing the coupling efficiency.

Alternatively, it is also possible to use the analytical solutions of the overlap integral given in Eqs. (9) and (10) with the correct beam parameters of the two modes. However, some of the beam parameters are not known and thus have to be obtained from the WPM simulation first. This is done by fitting Gaussian peaks to the radial electric field that is obtained from the WPM. The fit parameters yield the beam radius as a function of z. By fitting Eq. (2) to these results, the beam waist radius and its position are obtained. In addition to inaccurate beam parameters, the analytical results also do not include effects such as lens aberrations and diffraction. Thus, the numerical results are considered to be more precise. The results in Figs. 2(c) and (d) show that a lateral offset or tilt of the fiber relative to the fiber lens does not cause significant losses.

Optics EXPRESS

As expected, the smaller mode field diameter of the SM 780 HP results in higher losses due to lateral offsets but smaller losses due to tilts of the fiber. However, the latter effect is weakened as a result of the shorter wavelengths supported by the SM 780 HP which increases the losses created by the tilt (see Eq. (9)).

Aside from the lateral offset and the tilt of the fiber, further misalignments can be present in the lens system. They are illustrated in Fig. 3(a), with misalignments inside the lens system being measured at the apex of the fiber lens. As explained in subsection 2.3, this choice of the projection plane only influences the distribution of the losses between tilt and lateral offset. During the integration of the lensed fiber into the fiber holder, it can happen that the fiber is not fully inserted, but instead exhibits a longitudinal offset s_L. Additionally, the fiber can be tilted and/or shifted laterally within the fiber holder. Here, it is important that the amount of tilt and offset is limited by the inner radius of the fiber holder - which is typically about 0.5 µm larger than the outer radius of the fiber - and the length of the fiber holder which is assumed to be 280 µm, based on the design used in Ref. [37]. This means that if tilt and offset are considered simultaneously, the amount of tilt limits the possible lateral offset and vice versa. Maximum losses occur for a maximum tilt of $\theta_\mathrm{holder,max} \approx 0.2°$ which creates an offset of $\theta_\mathrm{holder,max} \cdot (l_\mathrm{holder}/2 + l_\mathrm{fiber\,lens})$ at the position of the fiber tip. Here, l_holder is the length of the inner part of the fiber holder and $l_\mathrm{fiber\,lens}$ is the length of the fiber lens. Of course, tilt and offset can be limited by increasing the size of the fiber holder. By assuming that the fiber lens is completely straight, the maximum possible tilt of the fiber can theoretically vanish and the maximum lateral offset will approach 0.5 µm.

Moreover, the tilt and offset of the fiber lens is also influenced by the cleaving angle of the fiber θ_F which was already introduced. When the fiber is assumed to be at the right position, the fiber lens will be tilted by the angle of θ_F and shifted laterally by $\theta_\mathrm{F} \cdot l_\mathrm{fiber\,lens}$. Thus, the cleaving angle can influence the tilt and offset of the fiber lens and is therefore important to estimate their typical values. However, we want to point out that the losses that are created by the cleaving angle at the fiber tip are not considered in these results.

The tilt of the fiber and the cleaving angle, as well as the different lateral offsets that can arise, add up to the absolute values of θ_L and d_L (denoted as d_L2 for the doublet lens designs) at the vertex of the fiber lens. On that note, it is of course possible that the individual angles or offsets are oriented in different directions and partially cancel each other out. More information on the size of the offsets created by the tilt of the lensed fiber and the cleaving angle is given in Supplement 1.

Another possible misalignment for doublet lens designs is a lateral shift of the substrate lens in regard to the SPS. This case is mathematically equivalent to the lateral shift of the lensed fiber for singlet lens designs.

The effects for these misalignments are estimated similarly to the previous case with few adaptations made for the numerical solutions. The easiest way to treat misalignments inside the lens system is by implementing the adjusted lens design in the WPM simulation. Thus, a longitudinal offset of the fiber lens can be implemented by shifting the position of the fiber lens. After that, the coupling efficiency can be evaluated at the new position of the fiber tip. However, a lateral offset or tilt inside the lens can not be implemented in the same way due to the limitation to rotational symmetric lens systems in this implementation of the WPM. Therefore, the coupling efficiency cannot be obtained at the position of the fiber tip in this case. This means that instead, the mode emitted by the fiber needs to be propagated through the fiber lens and into the air-filled gap between fiber and substrate lens. Subsequently, tilt and offset can again be added by shifting one of the modes or multiplying it by a factor of $\exp(ik\theta x)$. The analytical results are again obtained from Eqs. (8), (9), and (10) with the beam parameters of the modes at the corresponding position.

The simulation results show that considering realistic misalignment values (see Fig. 3), *doublet lens designs are superior to singlet lens designs*. In general, singlet lenses suffer from significantly

Optics EXPRESS

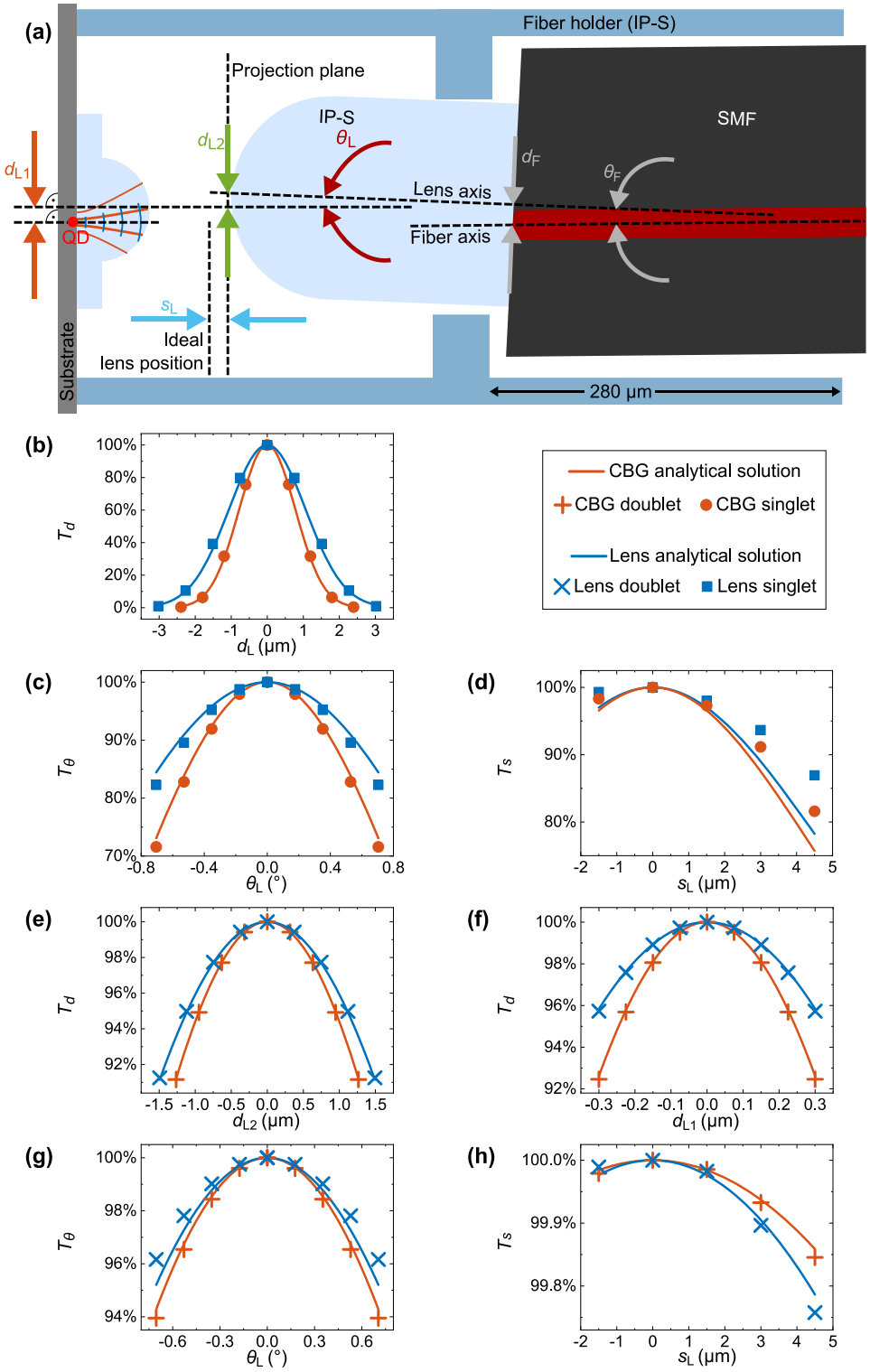

Fig. 3. (a) Schematic of all possible misalignments within the lens design shown exemplarily for a doublet lens design. (b)–(h) Normalized coupling efficiencies for circular Bragg grating (CBG) and microlens (lens) emitters: (b) singlet lenses and lateral offsets, (c) singlet lenses and tilt, (d) singlet lenses and longitudinal offsets, (e) doublet lenses and lateral offset of the fiber lens, (f) doublet lenses and lateral offset of the substrate lens, (g) doublet lenses and tilt, and (h) doublet lenses and longitudinal offsets.

Optics EXPRESS

higher losses as a result of the mode in the air-filled gap, where most misalignments occur, having a very small beam waist and high NA. The smaller beam waist results in an increased sensitivity to lateral and longitudinal offsets and thus results in higher losses (see Figs. 3(b) and (d)). Since the tilt is measured at the vertex of the fiber lens far away from the beam waists, the effect of the tilt is also increased for smaller beam waists. This again causes high losses for singlet lens designs as shown in Fig. 3(c).

A second lens printed onto the semiconductor substrate creates an additional misalignment component equivalent to the lateral offset of the lensed fiber for singlet lens designs. However, since the lateral offset caused by the printing process is smaller than the possible lateral offset of the fiber lens, the effects of a lateral shift of the semiconductor substrate relative to the substrate lens and the fiber holder are rather small (see Fig. 3(f)). In return for this additional loss, the beam waist in the air-filled gap is much larger. This limits the amount of loss that is created by a lateral offset of the modes and therefore decreases the amount of loss for both an offset and a tilt of the fiber lens (see Figs. 3(e) and (g)). Additionally, typical amounts of lateral offsets are decreased because of the much smaller size of the fiber lens. Since the beam in the air-filled gap has a low divergence as shown in Fig. 2(a), the longitudinal phase $\exp\left(-ik\rho^2/(2R(z))\right)$ (see Eq. (1)) of the mode changes very slowly. Therefore, the effects of a longitudinal shift of the lensed fiber become negligibly small (see Fig. 3(h)).

The previous results consider one single misalignment each. When combining various misalignments, it is important that only misalignments which are computed at the same projection plane can be considered in a single numerical simulation due to the limitation to rotationally symmetric lens designs. This means that at the fiber tip, the vertex of the fiber lens, and for doublet lens designs at the position of the QD, tilt and offsets can be combined in the numerical calculations. The obtained coupling efficiencies at these positions can then be multiplied to estimate the total coupling efficiency that takes every misalignment into account. The calculated coupling efficiencies for three different combinations of misalignments are given in Table 2.

3.4. Thermal effects

Since single-photon operation of the QD requires cryogenic temperatures, one has to consider the influence of temperature on the parameters of the lens system. This includes the refractive index of the lens material, due to the thermo optical effect [50] and the dimensions of the lenses due to volume shrinkage.

At very low temperatures, the linear thermal expansion coefficient α of the photoresist approaches zero. Between 4 K and room temperature (RT), we assume a linear behavior of α with a value of $\alpha_{\mathrm{RT}} \approx 90\,\mathrm{ppm/K}$ at RT [51]. That is, the temperature difference of $\Delta T \approx -300\,\mathrm{K}$ will lead to a shrinkage of every connected section of the lens design by a factor of

$$c_T = \frac{L + \Delta L}{L} = 1 + \frac{1}{2}\alpha_{\mathrm{RT}} \cdot \Delta T \approx 0.9865. \tag{11}$$

Additionally, the curvature of the lenses need to be adjusted. Thus, the aspheric lens equation $z_{\mathrm{L}}(\rho)$ which describes the curvature of an interface at RT is now given by $z'_{\mathrm{L}}(\rho) = z_{\mathrm{L}}\left(\rho/c_{\mathrm{T}}\right) \cdot c_{\mathrm{T}}$ at $T = 4\,\mathrm{K}$.

The temperature dependency of the refractive index n of the photoresist at RT is given by $\mathrm{d}n/\mathrm{d}T \approx -1.33 \cdot 10^{-4}$ [52]. By assuming the same linear behavior between 4 K and RT as for the thermal expansion coefficient, the total change of the refractive index can be calculated to

$$\Delta n = \frac{1}{2}\left(\frac{\mathrm{d}n}{\mathrm{d}T}\right)_{\mathrm{RT}} \cdot \Delta T \approx 0.02. \tag{12}$$

The coupling efficiency at 4 K for various values of c_{T} and Δn can be seen in Fig. 4. Because of the combined shrinkage of the fiber holder and the lenses, which are made out of the same

Optics EXPRESS

material, all linear dimensions of the lens design, including the focal length of the system, are scaled down. This explains why the shrinkage has only little effects on the coupling efficiency of singlet and doublet lens designs as shown in Fig. 4(a). A higher refractive index, on the other hand, likewise decreases the focal length of a single lens. But since the dimensions of the lens systems are not influenced in this case, this leads to higher losses as shown in Fig. 4(b). While coupling efficiencies only decrease slightly for the doublet lens designs with expected losses of less than 1%, the change of the refractive index has a big impact on the coupling efficiencies of the singlet lens designs with expected losses of 9% for the CBG and 14% for the microlens emitter. This is mainly because the change of the refractive index is more pronounced for interfaces of stronger refraction. Thus, the change of the refractive index has a larger effect for singlet lens designs and SPS and fibers with larger NA. This becomes clear when the emitters at all different wavelengths are compared. The supporting data is given in Supplement 1.

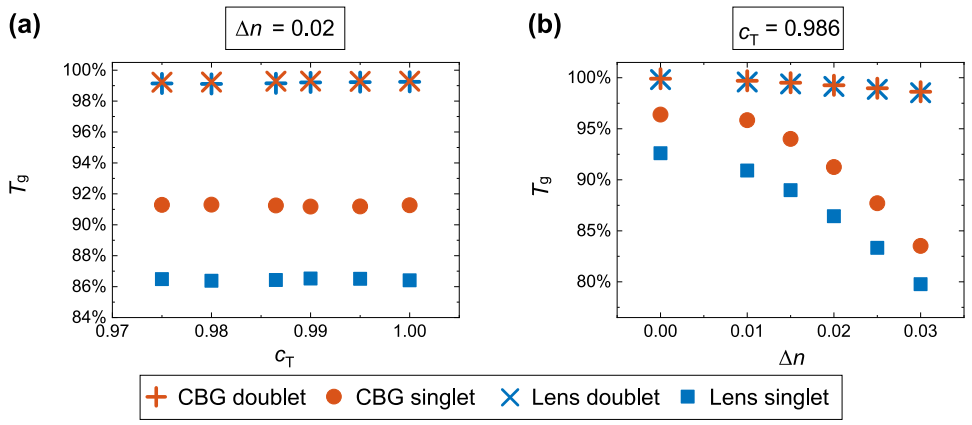

Fig. 4. Coupling efficiency of circular Bragg grating (CBG) and microlens (lens) emitters for various values of the linear thermal expansion coefficient c_T and the change of the refractive index Δn. In (a) the thermal expansion coefficient is varied while a change of the refractive index of $\Delta n = 0.02$ is assumed and in (b), the change of the refractive index is varied while the thermal expansion coefficient is set to $c_T = 0.9865$.

If the values of c_T and Δn were known accurately, one could compensate the effects of the temperature difference already while designing the lens system. To that end, the refractive index at 4 K needs to be used while designing the lens system. Furthermore, every connected section of the new lens design has to be divided by c_T resulting in the aspheric lens equation $z_{L,comp.}(\rho) = z_L(c_T \cdot \rho)/c_T$ for the final design. We want to point out that the fiber and the GaAs substrate on which the lenses are printed shrink differently compared to the photoresist. This can induce strain that changes the optical properties of the photoresist in this regime and might also cause a partial detachment of the lenses. The exact implications of this are part of our current experimental research.

4. Conclusion

We showed that single-photon sources with Gaussian like far-field emission pattern can theoretically be far field coupled into a single-mode fiber in a very efficient manner by using 3D-printed microoptics. To this end, singlet and doublet lens designs were created for semiconductor quantum dot sources based on circular Bragg gratings and microlenses at 930 nm an 1550 nm, respectively. By introducing various possible alignment errors in the design of the optical systems, it was shown that a tilt of the lensed fiber inside the fiber holder and the cleaving angle of the fiber are the most significant sources of potential losses due to mechanical misalignments. When

Optics EXPRESS

comparing singlet and doublet lens designs, we found that the inclusion of an additional lens printed on the semiconductor substrate significantly reduces the effects of a tilt or offset inside the lens system. While maximum values of the misalignments can potentially cause losses of up to 100% for singlet lens designs, the maximum losses for the doublet lens designs in this work is limited to less than 20%. We therefore conclude that doublet lens systems are preferable for most fiber coupling applications, while singlet designs should only be used when printing directly onto the emitter is not feasible. We also found that emitters and fibers with a large beam waist and small NA are less susceptible to misalignments. Since semiconductor quantum dots need to be cooled down to cryogenic temperatures in order to be operational as single-photon emitters, we also investigated the thermal effects on the coupling efficiency. While thermal shrinkage by itself does not have a significant influence on the coupling efficiency, the thermo-optical effect can cause high losses, especially for singlet lens designs. These losses, however, can be limited substantially by changing to doublet lens systems. In principle, thermo-optical losses can be avoided completely by adjusting the refractive index to the low-temperature value during the lens design.

Funding. Bundesministerium für Bildung und Forschung (Q.Link.X, QR.X); European Commission (PoC 3DPrintedOptics); Deutsche Forschungsgemeinschaft (GRK2642).

Disclosures. The authors declare no conflicts of interest.

Data availability. Data underlying the results presented in this paper are not publicly available at this time but may be obtained from the authors upon reasonable request.

Supplemental document. See Supplement 1 for supporting content.

References

1. J. L. O'Brien, A. Furusawa, and J. Vučković, "Photonic quantum technologies," Nat. Photonics **3**(12), 687–695 (2009).
2. J. Wang, F. Sciarrino, A. Laing, and M. G. Thompson, "Integrated photonic quantum technologies," Nat. Photonics **14**(5), 273–284 (2020).
3. W. J. Munro, K. Azuma, K. Tamaki, and K. Nemoto, "Inside Quantum Repeaters," IEEE J. Sel. Top. Quantum Electron. **21**(3), 78–90 (2015).
4. P. van Loock, W. Alt, C. Becher, O. Benson, H. Boche, C. Deppe, J. Eschner, S. Höfling, D. Meschede, P. Michler, F. Schmidt, and H. Weinfurter, "Extending Quantum Links: Modules for Fiber- and Memory-Based Quantum Repeaters," Adv. Quantum Technol. **3**(11), 1900141 (2020).
5. F. Basso Basset, M. B. Rota, C. Schimpf, D. Tedeschi, K. D. Zeuner, S. F. Covre da Silva, M. Reindl, V. Zwiller, K. D. Jöns, A. Rastelli, and R. Trotta, "Entanglement Swapping with Photons Generated on Demand by a Quantum Dot," Phys. Rev. Lett. **123**(16), 160501 (2019).
6. F. Xu, X. Ma, Q. Zhang, H.-K. Lo, and J.-W. Pan, "Secure quantum key distribution with realistic devices," Rev. Mod. Phys. **92**(2), 025002 (2020).
7. C. Schimpf, M. Reindl, D. Huber, B. Lehner, S. F. C. D. Silva, S. Manna, M. Vyvlecka, P. Walther, and A. Rastelli, "Quantum cryptography with highly entangled photons from semiconductor quantum dots," Sci. Adv. **7**(16), eabe8905 (2021).
8. H. Wang, Y.-M. He, T.-H. Chung, H. Hu, Y. Yu, S. Chen, X. Ding, M.-C. Chen, J. Qin, X. Yang, R.-Z. Liu, Z.-C. Duan, J.-P. Li, S. Gerhardt, K. Winkler, J. Jurkat, L.-J. Wang, N. Gregersen, Y.-H. Huo, Q. Dai, S. Yu, S. Höfling, C.-Y. Lu, and J.-W. Pan, "Towards optimal single-photon sources from polarized microcavities," Nat. Photonics **13**(11), 770–775 (2019).
9. G. Bulgarini, M. E. Reimer, M. Bouwes Bavinck, K. D. Jöns, D. Dalacu, P. J. Poole, E. P. A. M. Bakkers, and V. Zwiller, "Nanowire Waveguides Launching Single Photons in a Gaussian Mode for Ideal Fiber Coupling," Nano Lett. **14**(7), 4102–4106 (2014).
10. F. Flamini, N. Spagnolo, and F. Sciarrino, "Photonic quantum information processing: a review," Rep. Prog. Phys. **82**(1), 016001 (2018).
11. P. Senellart, G. Solomon, and A. White, "High-performance semiconductor quantum-dot single-photon sources," Nat. Nanotechnol. **12**(11), 1026–1039 (2017).
12. D. Hunger, T. Steinmetz, Y. Colombe, C. Deutsch, T. W. Hänsch, and J. Reichel, "A fiber Fabry–Perot cavity with high finesse," New J. Phys. **12**(6), 065038 (2010).
13. I. Aharonovich, D. Englund, and M. Toth, "Solid-state single-photon emitters," Nat. Photonics **10**(10), 631–641 (2016).

Optics EXPRESS

14. D. Riedel, I. Söllner, B. J. Shields, S. Starosielec, P. Appel, E. Neu, P. Maletinsky, and R. J. Warburton, "Deterministic Enhancement of Coherent Photon Generation from a Nitrogen-Vacancy Center in Ultrapure Diamond," Phys. Rev. X **7**, 031040 (2017).
15. H. Kaupp, T. Hümmer, M. Mader, B. Schlederer, J. Benedikter, P. Haeusser, H.-C. Chang, H. Fedder, T. W. Hänsch, and D. Hunger, "Purcell-Enhanced Single-Photon Emission from Nitrogen-Vacancy Centers Coupled to a Tunable Microcavity," Phys. Rev. Appl. **6**(5), 054010 (2016).
16. A. Sipahigil, R. E. Evans, D. D. Sukachev, M. J. Burek, J. Borregaard, M. K. Bhaskar, C. T. Nguyen, J. L. Pacheco, H. A. Atikian, C. Meuwly, R. M. Camacho, F. Jelezko, E. Bielejec, H. Park, M. Loncar, and M. D. Lukin, "An integrated diamond nanophotonics platform for quantum-optical networks," Science **354**(6314), 847–850 (2016).
17. C. Chakraborty, N. Vamivakas, and D. Englund, "Advances in quantum light emission from 2D materials," Nanophotonics **8**(11), 2017–2032 (2019).
18. S. Ritter, C. Nölleke, C. Hahn, A. Reiserer, A. Neuzner, M. Uphoff, M. Mücke, E. Figueroa, J. Bochmann, and G. Rempe, "An elementary quantum network of single atoms in optical cavities," Nature **484**(7393), 195–200 (2012).
19. C. Monroe, R. Raussendorf, A. Ruthven, K. R. Brown, P. Maunz, L.-M. Duan, and J. Kim, "Large-scale modular quantum-computer architecture with atomic memory and photonic interconnects," Phys. Rev. A **89**(2), 022317 (2014).
20. Y. Arakawa and M. J. Holmes, "Progress in quantum-dot single photon sources for quantum information technologies: A broad spectrum overview," Appl. Phys. Rev. **7**(2), 021309 (2020).
21. J. Claudon, J. Bleuse, N. S. Malik, M. Bazin, P. Jaffrennou, N. Gregersen, C. Sauvan, P. Lalanne, and J.-M. Gérard, "A highly efficient single-photon source based on a quantum dot in a photonic nanowire," Nat. Photonics **4**(3), 174–177 (2010).
22. M. Munsch, N. S. Malik, E. Dupuy, A. Delga, J. Bleuse, J.-M. Gérard, J. Claudon, N. Gregersen, and J. Mørk, "Dielectric GaAs Antenna Ensuring an Efficient Broadband Coupling between an InAs Quantum Dot and a Gaussian Optical Beam," Phys. Rev. Lett. **110**(17), 177402 (2013).
23. A. Musiał, K. Żołnacz, N. Srocka, O. Kravets, J. Große, J. Olszewski, K. Poturaj, G. Wójcik, P. Mergo, K. Dybka, M. Dyrkacz, M. Dłubek, K. Lauritsen, A. Bülter, P.-I. Schneider, L. Zschiedrich, S. Burger, S. Rodt, W. Urbańczyk, G. Sęk, and S. Reitzenstein, "Plug&Play Fiber-Coupled 73 kHz Single-Photon Source Operating in the Telecom O-Band," Adv. Quantum Technol. **3**(6), 2000018 (2020).
24. M. Anderson, T. Müller, J. Huwer, J. Skiba-Szymanska, A. B. Krysa, R. M. Stevenson, J. Heffernan, D. A. Ritchie, and A. J. Shields, "Quantum teleportation using highly coherent emission from telecom C-band quantum dots," npj Quantum Information **6**(1), 14 (2020).
25. R. Sittig, C. Nawrath, S. Kolatschek, S. Bauer, R. Schaber, J. Huang, P. Vijayan, P. Pruy, S. L. Portalupi, M. Jetter, and P. Michler, "Thin-film InGaAs metamorphic buffer for telecom C-band InAs quantum dots and optical resonators on GaAs platform," Nanophotonics **11**(6), 1109–1116 (2022).
26. T. Gao, L. Rickert, F. Urban, J. Große, N. Srocka, S. Rodt, A. Musiał, K. Żołnacz, P. Mergo, K. Dybka, W. Urbańczyk, G. Sęk, S. Burger, S. Reitzenstein, and T. Heindel, "A quantum key distribution testbed using a plug&play telecom-wavelength single-photon source," Appl. Phys. Rev. **9**(1), 011412 (2022).
27. J.-H. Kim, T. Cai, C. J. K. Richardson, R. P. Leavitt, and E. Waks, "Two-photon interference from a bright single-photon source at telecom wavelengths," Optica **3**(6), 577–584 (2016).
28. J. Yang, C. Nawrath, R. Keil, R. Joos, X. Zhang, B. Höfer, Y. Chen, M. Zopf, M. Jetter, S. L. Portalupi, F. Ding, P. Michler, and O. G. Schmidt, "Quantum dot-based broadband optical antenna for efficient extraction of single photons in the telecom O-band," Opt. Express **28**(13), 19457–19468 (2020).
29. L. Bremer, C. Jimenez, S. Thiele, K. Weber, T. Huber, S. Rodt, A. Herkommer, S. Burger, S. Höfling, H. Giessen, and S. Reitzenstein, "Numerical optimization of single-mode fiber-coupled single-photon sources based on semiconductor quantum dots," Opt. Express **30**(10), 15913–15928 (2022).
30. P.-I. Schneider, N. Srocka, S. Rodt, L. Zschiedrich, S. Reitzenstein, and S. Burger, "Numerical optimization of the extraction efficiency of a quantum-dot based single-photon emitter into a single-mode fiber," Opt. Express **26**(7), 8479–8492 (2018).
31. L. Rickert, T. Kupko, S. Rodt, S. Reitzenstein, and T. Heindel, "Optimized designs for telecom-wavelength quantum light sources based on hybrid circular Bragg gratings," Opt. Express **27**(25), 36824–36837 (2019).
32. S. A. Blokhin, M. A. Bobrov, N. A. Maleev, J. N. Donges, L. Bremer, A. A. Blokhin, A. P. Vasil'ev, A. G. Kuzmenkov, E. S. Kolodeznyi, V. A. Shchukin, N. N. Ledentsov, S. Reitzenstein, and V. M. Ustinov, "Design optimization for bright electrically-driven quantum dot single-photon sources emitting in telecom O-band," Opt. Express **29**(5), 6582–6598 (2021).
33. J. K. Hohmann, M. Renner, E. H. Waller, and G. von Freymann, "Three-Dimensional μ-Printing: An Enabling Technology," Adv. Opt. Mater. **3**(11), 1488–1507 (2015).
34. J. Fischer and M. Wegener, "Three-dimensional optical laser lithography beyond the diffraction limit," Laser Photonics Rev. **7**(1), 22–44 (2013).
35. P.-I. Dietrich, M. Blaicher, I. Reuter, M. Billah, T. Hoose, A. Hofmann, C. Caer, R. Dangel, B. Offrein, U. Troppenz, M. Moehrle, W. Freude, and C. Koos, "In situ 3D nanoprinting of free-form coupling elements for hybrid photonic integration," Nat. Photonics **12**(4), 241–247 (2018).
36. T. Gissibl, S. Thiele, A. Herkommer, and H. Giessen, "Sub-micrometre accurate free-form optics by three-dimensional printing on single-mode fibres," Nat. Commun. **7**(1), 11763 (2016).

Optics EXPRESS

37. L. Bremer, K. Weber, S. Fischbach, S. Thiele, M. Schmidt, A. Kaganskiy, S. Rodt, A. Herkommer, M. Sartison, S. L. Portalupi, P. Michler, H. Giessen, and S. Reitzenstein, "Quantum dot single-photon emission coupled into single-mode fibers with 3D printed micro-objectives," APL Photonics **5**(10), 106101 (2020).
38. M. Sartison, K. Weber, S. Thiele, L. Bremer, S. Fischbach, T. Herzog, S. Kolatschek, M. Jetter, S. Reitzenstein, A. Herkommer, P. Michler, S. L. Portalupi, and H. Giessen, "3D printed micro-optics for quantum technology: Optimised coupling of single quantum dot emission into a single-mode fibre," Light: Adv. Manuf. **2**, 103 (2021).
39. B. E. A. Saleh and M. C. Teich, *Fundamentals of Photonics* (John Wiley & Sons, Ltd., 1991), Chap. 3, pp. 80–107.
40. A. E. Siegman, *Lasers* (University Science Books, 1986), Chap. 17, 20, pp. 663–685, 782–786.
41. W. D. Joo, "Propagation of a general Gaussian beam by paraxial ray tracing in an arbitrary optical system," J. Korean Phys. Soc. **58**(4), 735–741 (2011).
42. S. Schmidt, S. Thiele, A. Herkommer, A. Tünnermann, and H. Gross, "Rotationally symmetric formulation of the wave propagation method-application to the straylight analysis of diffractive lenses," Opt. Lett. **42**(8), 1612–1615 (2017).
43. K. H. Brenner and W. Singer, "Light propagation through microlenses: a new simulation method," Appl. Opt. **32**(26), 4984–4988 (1993).
44. D. Marcuse, "Gaussian approximation of the fundamental modes of graded-index fibers," J. Opt. Soc. Am. **68**(1), 103–109 (1978).
45. W. B. Joyce and B. C. DeLoach, "Alignment of Gaussian beams," Appl. Opt. **23**(23), 4187–4196 (1984).
46. D. Marcuse, "Loss Analysis of Single-Mode Fiber Splices," Bell Syst. Tech. J. **56**(5), 703–718 (1977).
47. K. Weber, "3D Printed Micro-Optics: Materials, Methods and Applications," Ph.D. thesis (University of Stuttgart, 2022).
48. K. Ott, S. Garcia, R. Kohlhaas, K. Schüppert, P. Rosenbusch, R. Long, and J. Reichel, "Millimeter-long fiber Fabry-Perot cavities," Opt. Express **24**(9), 9839–9853 (2016).
49. M. A. A. Mamun, P. J. Cadusch, T. Katkus, S. Juodkazis, and P. R. Stoddart, "Quantifying end-face quality of cleaved fibers: Femtosecond laser versus mechanical scribing," Opt. Laser Tech. **141**, 107111 (2021).
50. E. D. Palik, ed., *Handbook of Optical Constants of Solids* (Academic Press, 1997), Chap. 3 - Thermo-Optic Coefficients, pp. 115–261.
51. M. Esposito, S. Buontempo, A. Petriccione, M. Zarrelli, G. Breglio, A. Saccomanno, Z. Szillasi, A. Makovec, A. Cusano, A. Chiuchiolo, M. Bajko, and M. Giordano, "Fiber Bragg Grating sensors to measure the coefficient of thermal expansion of polymers at cryogenic temperatures," Sensors Actuators A: Phys. **189**, 195–203 (2013).
52. G. Beadie, M. Brindza, and R. Flynn, "Refractive index measurements of polymethyl methacrylate (PMMA) from 0.4-1.6 µm," Appl. Opt. **54**(31), F139 (2015).

129.69.22.154 {ts '2024-01-08 09:02:05'}